1 **Revision 1**

# 2 Measurements of the Lamb-Mössbauer factor at simultaneous high-
# 3 pressure-temperature conditions and estimates of the equilibrium isotopic
# 4 fractionation of iron

5 Dongzhou Zhang[1,4], Jennifer M. Jackson[2], Wolfgang Sturhahn[2], Jiyong Zhao[3], E. Ercan Alp[3],
6 Michael Y. Hu[3]
7 [1]Hawaii Institute of Geophysics and Planetology, University of Hawaii at Manoa, Honolulu,
8 Hawaii 96822
9 [2]Seismological Laboratory, California Institute of Technology, Pasadena, California 91125
10 [3]Advanced Photon Source, Argonne National Laboratory, Argonne, Illinois 60439
11 [4]GSECARS, University of Chicago, Argonne, Illinois 60439
12
13 **Abstract**
14

Isotopic fractionation has been linked to the lattice vibrations of materials through their phonon spectra. The Lamb-Mössbauer factor ($f_{LM}$) has the potential to provide information about the lattice vibrations in materials. We constrain the temperature evolution of the $f_{LM}$ of $\gamma$- and $\epsilon$-Fe at *in-situ* high P-T conditions between 1650 K and the melting point. We find that the vibrations of $\gamma$- and $\epsilon$-Fe can be described using a quasiharmonic model with a pressure and temperature dependent Debye temperature computed from the measured $f_{LM}$. From the Debye temperature, we derive the equilibrium isotopic fractionation $\beta$-factor of iron. Our results show that the quasiharmonic behavior of metallic iron would lower the value of $\ln\beta_{\mathrm{Fe}}^{57/54}$ by 0.1‰ at 1600-2800 K and 50 GPa when compared to the extrapolation of room temperature nuclear resonant inelastic X-ray scattering data. Our study suggests that anharmonicity may be more prevalent in Fe metal than in lower mantle minerals at 2800 K and 50 GPa, a relevant condition for the core formation, and the silicate mantle may be isotopically heavy in iron.

## 1. Introduction

Studies of the collective atomic oscillations in crystalline materials, or quantized lattice vibrations (phonons), are important for understanding and predicting the behavior of earth materials (e.g, Reynard et al. 2015). For example, acoustic phonons at the long-wavelength limit are intricately related to the elastic properties of minerals and affect seismic wave propagation within the earth (Lin et al. 2005; Sturhahn and Jackson 2007; Zhang et al. 2013; Murphy et al. 2013; Chen et al. 2014; Wicks et al. 2017). Measurements of the phonon density of states as a function of pressure provide constraints on important thermodynamic parameters, including the vibrational free energy, entropy, and kinetic energy (e.g., Murphy et al. 2013; Morrison et al. 2019). Understanding phonon

behavior in minerals provides estimates on the thermal budget of the earth, as heat is mainly stored and transported via vibrational excitations (Chai et al. 1996; Jeanloz and Morris 1986; Jeanloz and Richter 1979; Kieffer 1979a, 1979b, 1979c, 1980, 1982). Studies of lattice vibrations have led to a better understanding of phase transitions (e.g., Wentzcovitch et al. 2010; Yu et al. 2008; Yu et al. 2010), including melting (Shen and Heinz 1998; Alfè et al. 1999, 2002, 2004; Vočadlo and Alfe 2002). Geochemical studies have demonstrated that mantle derived rocks are ~0.1‰ heavier in $\delta^{57}$Fe than chondrite (Poitrasson et al. 2004; Sossi et al. 2016), and measurements of lattice vibrational properties of minerals and glasses are used to constrain whether the core formation would leave such isotopic signature to mantle rocks (Polyakov 2009; Shahar et al. 2016; Liu et al. 2017).

Lattice vibrations are determined by the interatomic potential (e.g., Reynard et al. 2015; Fultz 2010). In the harmonic approximation, the interatomic potential is quadratic in the vicinity of the atomic equilibrium positions (e.g., Dunitz et al. 1988; Trueblood et al. 1996; Sturhahn and Jackson 2007; Reynard et al. 2015). The harmonic approximation assumes that phonon spectra do not change with temperature. Although the harmonic approximation is used to explain select physical properties of some solids under particular conditions (mostly at low temperatures), this model often fails to explain or predict material behavior under a wide range of conditions (Polyakov 1998; Fultz 2010; Wu 2010; Mauger et al. 2014). Several components contribute to the deviation from harmonicity in solids and are described by different physical models. Often-used models to describe nonharmonic lattice vibrations are quasiharmonic approximations, which allow temperature- and/or pressure-induced volume changes while assuming harmonic, non-interacting phonons (Polyakov 1998; Fultz 2010; Wu 2010; Mauger et al. 2014; Allen 2020).

Under some conditions, particularly at high temperatures, higher order terms of the interatomic potential are required to describe the atomic displacements and the anharmonicity is dominated by phonon-phonon interactions. These effects are sometimes named "intrinsic anharmonicity" (Polyakov 1998; Sturhahn and Jackson 2007; Fultz 2010; Reynard et al. 2015; Bansal et al. 2016; Allen 2020). In addition to phonon-phonon interactions, electron-phonon and magnon-phonon interactions might be included in the description of "intrinsic anharmonicity" (Fultz 2010; Mauger et al. 2014; Bansal et al. 2016). Anharmonicity is the origin of several important physical properties in solids, such as thermal expansion and lattice thermal conductivity (e.g., Reynard et al. 2015) and various other experimentally observable effects (Tse et al. 2005; Brown 1969; Chumakov et al. 1996; Mauger et al. 2014; Kim et al. 2018).

Here we assume weak anharmonicity which permits us to use a quasiharmonic model for the lattice vibrations. A description of the lattice vibrations via the phonon density of states (DOS) can be determined experimentally, e.g., by inelastic X-ray/neutron scattering or nuclear resonant inelastic X-ray scattering. However in many cases, a contraction of the DOS, such as specific heat or mean-square atomic displacement, is experimentally accessible. Our data provide us with the Lamb-Mössbauer factor of hot compressed iron, which for our quasiharmonic model is related to the mean-square displacement of the iron atoms

$$\langle u^2 \rangle = -\frac{1}{k_0^2} \ln f_{LM}, \quad (1)$$

where $k_0$ = 7.306 Å$^{-1}$ is the wavenumber of the 14.4125 keV X-rays which corresponds to the nuclear resonant energy level of iron (Sturhahn 2004). The atomic mean square displacement $\langle u^2 \rangle$ is the quantum-mechanical time-average of the square of atomic displacement with respect to its equilibrium position (Singwi and Sjölander 1960; Sturhahn and Chumakov 1999), and the close relationship between the atomic mean square displacement $\langle u^2 \rangle$ and the DOS has been described earlier (Singwi and Sjölander 1960; Dunitz et al. 1988; Trueblood et al. 1996; Sturhahn and Chumakov 1999). A harmonic model gives a linear temperature behavior for sufficiently high temperatures $\lim_{T\to\infty} \langle u^2 \rangle \propto T$. Deviations from this asymptotic linearity are interpreted as resulting from anharmonicity.

Using Mössbauer spectroscopy data, the equilibrium isotopic fractionation $\beta$-factor was first estimated from the second order Doppler shift (Polyakov 1997; Polyakov and Mineev 2000). More recently, using nuclear resonant inelastic X-ray scattering (NRIXS), the general moments (GM) method has been developed to estimate the iron isotopic fractionation between minerals from their lattice vibrational properties (Polyakov et al. 2007; Polyakov 2009; Dauphas et al. 2012, 2018). In the GM method, the equilibrium isotopic fractionation $\beta$-factor of each mineral is calculated either from the moments of the iron nuclear resonant inelastic X-ray scattering spectrum (Polyakov et al. 2007; Polyakov 2009), or from the mean force constants (stiffness) derived from the iron partial phonon DOS (Dauphas et al. 2012; Shahar et al. 2016; Liu et al. 2017), or both (Murphy et al. 2013; Dauphas et al. 2018). A few recent studies have used this GM approach to estimate the iron isotopic fingerprints on the bulk silicate earth during the core-formation process (Shahar et al. 2016; Liu et al. 2017). Most of the research using the GM approach extrapolate room temperature NRIXS results to high temperatures, without considering deviations from harmonicity. Studies

have suggested that the deviation from harmonicity of lattice vibrations lowers the $\beta$-factor, and that the quasiharmonic correction has a more pronounced effect than the intrinsic anharmonic component (Polyakov 1998, 2009).

Mössbauer spectroscopy is a suitable method to measure the Lamb-Mössbauer factor, which is the probability of recoilless scattering of nuclear resonant X-rays, under various experimental conditions (Sturhahn, 2004; Sturhahn and Jackson, 2007). One can calculate the temperature dependence of $\langle u^2 \rangle$ from the temperature dependence of $f_{LM}$ using Eq. 1. $f_{LM}$ varies with material composition, lattice or local atomic structure, and experimental conditions, such as temperature or pressure (Bergmann et al. 1994; Chumakov et al. 1996; Shen et al. 2004; Lin et al. 2005; Jackson et al. 2013; Zhang et al. 2016; Morrison et al. 2019). However, the relationship between Lamb-Mössbauer factor and isotopic fractionation has not been established and is presented here as an important innovation for the study of isotopic fractionation in solids at high temperatures.

The physical and chemical properties of iron at elevated pressure-temperature conditions are important to understand the internal structure and evolution of the earth. In addition to the liquid state, iron is known to have three major allotropes at elevated pressure-temperature conditions: the body-centered cubic ($\alpha$) phase, the face-centered cubic ($\gamma$) phase, and the hexagonal close-packing ($\epsilon$) phase. The $f_{LM}$ of $\alpha$-Fe has been measured at various temperatures from 4 to ~1300 K using conventional Mössbauer spectroscopy (Kolk et al. 1986; Kovats and Walker 1969), NRIXS (Chumakov and Sturhahn 1999; Mauger et al. 2014) and synchrotron Mössbauer spectroscopy (SMS) (Bergmann et al. (1994), room pressure only). The $f_{LM}$ of $\epsilon$-Fe has been studied with NRIXS up to 171 GPa at 300 K (Murphy et al. 2013; Morrison et al. 2019) and up to 73 GPa at

129 temperatures below 1700 K (Shen et al. 2004; Lin et al. 2005). Limited measurements on the $f_{LM}$
130 of $\gamma$-Fe have been carried out at room pressure (Kovats and Walker 1969; Mauger et al. 2014).
131 The $f_{LM}$ of $\gamma$-Fe has never been systematically studied at high-pressures. Measuring the $f_{LM}$ of iron
132 at temperatures above 1700 K is challenging using conventional Mössbauer spectroscopy and
133 NRIXS, because the recoil-free fraction decreases with temperature and it is very difficult to
134 maintain a stable uniform sample temperature over the long data collection times required to obtain
135 a statistically meaningful result (several hours to days).
136
137 We have measured the Lamb-Mössbauer factor of iron at elevated pressures and temperatures
138 using synchrotron Mössbauer spectroscopy. Our method combines the laser-heated diamond anvil
139 cell (DAC), the recently developed fast temperature readout spectrometer (FasTeR) for accurate
140 and precise temperature determinations, and the SMS technique to monitor the atomic dynamics
141 of the iron nuclei (Singwi and Sjölander, 1960; Boyle et al. 1961; Jackson et al. 2013; Zhang et al.
142 2015, 2016), while constraining the evolution of the effective thickness of the sample. This
143 approach is capable of determining the $f_{LM}$, and thus iron's atomic mean square displacement, up
144 to its melting point at elevated pressures. From the $f_{LM}$ data, we present a quasiharmonic correction
145 to iron's isotope fractionation β-factor at elevated pressure-temperature conditions, and discuss its
146 potential geochemical implications to earth's core formation process.
147
148 **2. Experiments to determine the Lamb-Mössbauer factor at high P-T conditions**
149
150 In our experiment, a symmetric DAC is used to provide the high pressure environment. Two Type-
151 I diamonds with 300 $\mu$m culet are mounted and aligned to form the anvils. A Re gasket is pre-

indented to ~45 $\mu$m thick, and a 115 $\mu$m diameter hole is drilled in the center of the pre-indention using a laser drilling system. A 95% isotopically enriched $^{57}$Fe foil with 3 $\mu$m thickness is cut into a $70 \times 70 \mu m^2$ square section and cleaned. Note the $^{57}$Fe samples used here are from the same larger foil used in previous studies (Jackson et al. 2013; Murphy et al. 2013; Zhang et al. 2016). Dehydrated KCl is pressed into transparent flakes and loaded together with the foils in a sandwich configuration into the Re gasket. The KCl serves as both a pressure-transmitting medium and thermal insulator. The DAC is heated in a vacuum furnace overnight before closing to remove the moisture.

The experiments are carried out at beamline 3-ID-B at the Advanced Photon Source, and the experimental setup is illustrated in Zhang et al. (2015). The storage ring is operated in low-emittance top-up mode with 24 bunches that are separated by 153 ns. The energy (14.4125 keV) and resolution (1 meV) of the X-rays are determined by a silicon high resolution monochromator (Toellner 2000), and a focus area of ~10 $\mu$m × 14 $\mu$m (full width at half maximum) is achieved by a Kirkpatrick-Baez mirror system. In-situ angular dispersive X-ray diffraction (XRD) patterns are collected at beamline 3-ID-B using 14.4125 keV X-ray to constrain the crystal symmetry and unit cell parameters, which are used to compute the pressure using the equation of state of iron (see below). A high resolution MAR image plate, located ~0.3 m downstream from the DAC, is used to collect the XRD patterns. Each XRD pattern is collected for ~30 min. A $CeO_2$ standard sample is used to calibrate the sample to image plate distance and correct the tilt of the image plate. The diffraction images are integrated into angular resolved intensity files using the DIOPTAS software (Prescher and Prakapenka 2015). In our experiments, $\epsilon$-Fe is observed in both runs at ambient temperature. The 300 K equations of state of $\epsilon$-Fe from Fei et al. (2016) are used to

175 calculate the pressure at room temperature. All the samples are laser-annealed at 1500 K for ~30
176 minutes before XRD measurements are collected, so as to release the residual deviatoric stress and
177 reduce the pressure gradient on the sample. After the heating run, we collect another XRD pattern
178 at 300 K to constrain any pressure drift. We report the pressure computed using the XRD
179 measurements at the sample location where heating experiment is applied. We estimate the thermal
180 contribution to the pressure using the empirical equation from our previous study utilizing a similar
181 sample configuration: $\Delta P = a(T - 300K) + c(T^2 - 90000K^2)$, where a = $4.6\times10^{-3}$ GPa/K, c
182 = $2\times10^{-6}$ $GPa^2/K^2$, and an additional 2 GPa is added to the pressure uncertainty in Tab. 1 due to
183 the scatter in the thermal pressure contribution (Zhang et al. 2016).
184
185 The experimental setup of the SMS measurement is similar to that of the XRD, and an avalanche
186 photodiode is placed ~0.5 m downstream from the sample (Zhang et al. 2015). As stated above,
187 the samples in each DAC are laser-annealed prior to the following experimental procedure. An
188 SMS spectrum is first collected at room-temperature (300 K) as a reference on the sample position
189 where the high temperature measurement will be carried out. The room-temperature SMS
190 spectrum provides two pieces of information: the time interval used to collect the time-resolved
191 SMS signal (also known as the timing window of the experiment, see Sturhahn 1999) and the
192 effective thickness of the sample before the series of high-temperature measurements. The profile
193 of the time resolved delayed counts, *S*, is a function depending on the level splitting of the resonant
194 nuclei and the effective thickness of the sample, $\eta$. The effective thickness is a dimension-less
195 number given as the product of the numerical density of the $^{57}$Fe nuclei, $\rho$, the physical thickness
196 of the sample, $d$, the nuclear resonant cross section, $\sigma = 2.56 \times 10^{-22}\mathrm{m}^2$, and the $f_{LM}$:
197

198 $$\eta = \rho d \sigma f_{LM}. \quad (2)$$

199

200 For $\gamma$- and $\epsilon$-Fe, it is known that the nuclear levels of $^{57}$Fe are unsplit (Macedo and Keune 1988).
201 Therefore, S reduces to:

202

203 $$S(t,\eta) = \eta^2 e^{-t/\tau} \frac{J_1^2(\sqrt{\eta t/\tau})}{\eta t/\tau}, \quad (3)$$

204

205 where $t$ is the time delay from the exciting X-ray bunch, $J_1$ is the first order Bessel function of the
206 first kind, and $\tau$ is the life time of the excited nuclear state (141 ns for $^{57}$Fe) (Sturhahn 2000;
207 Jackson et al. 2013). By fitting the room-temperature SMS spectrum with Eq. 3, the effective
208 thickness distribution at 300 K is obtained (Fig. 1). Since the $f_{LM}$ of $\epsilon$-Fe has been measured as a
209 function of pressure (Murphy et al. 2013), one can calculate the physical thickness distribution
210 from the effective thickness distribution.

211

212 The next step is to determine the effective thickness as a function of temperature, by monitoring
213 the temperature evolution of the integrated SMS signal (delayed counts). We proceed to heat both
214 sides of sample to 1650 K and balance the temperatures read from a charge-coupled device (CCD)
215 detector, so that the sample is heated uniformly (Jackson et al. 2013; Zhang et al. 2015, 2016). The
216 temperature difference of the upstream and downstream sides of sample is found to be smaller than
217 10 K. We collect a high temperature SMS spectrum and determine the effective thickness under
218 these conditions (Fig. 1). After the high temperature SMS measurement, we proceed with a
219 computer-acquisition program to ramp up the laser power until the sample melts, while
220 simultaneously monitoring the delayed counts, the temperature of the sample and the readings of

ion chambers (Jackson et al. 2013; Zhang et al. 2016). Each temperature is held for 3 seconds, which is enough for the sample to reach thermal relaxation and equilibration (Anzellini et al. 2013). The temperature of the sample is monitored by the FasTeR spectrometer and CCD detector (Zhang et al. 2015), and the reported temperature error incorporates the fluctuation of the ~300 FasTeR readings within the 3 seconds data collection time, and the estimated 10 K temperature difference between the upstream and downstream sides of the sample (Zhang et al. 2016). The melting point is determined from fits to the data set of normalized SMS delayed counts as a function of temperature using the MINUTI software package (Sturhahn 2020; Zhang et al. 2015). Due to the finite timing window, the delayed counts are not directly proportional to the effective thickness. The delayed counts are first normalized with the readings from ion chambers, which is proportional to the incident X-ray photon flux. Then, the normalized delayed counts are converted to effective thickness using the following equation (Fig. 2):

$$I(\eta) = Ae^{-\mu d} \sum_{n=0}^{\infty} \int_{t_1+nt_B}^{t_2+nt_B} S\,(t', \eta) dt', \quad (4)$$

where $t_1$ and $t_2$ are the beginning and end of the time window accessible from the SMS spectrum, $t_B$ is the time interval between X-ray pulses given by the synchrotron operation mode (in our case $t_B$=153 ns), $A$ is a scaling factor that depends on experimental conditions such as spectral X-ray flux incident on the sample, $d$ is the physical thickness of the sample, $\mu$ is the electronic absorption coefficient of the sample material, $S$ is the profile of time resolved delayed counts described in Eq. 3, and $\eta$ is the effective thickness of the sample (Jackson et al. 2013). In the data fitting, the starting effective thickness is constrained from the 1650 K SMS spectrum, and the effective thickness at the melting point is fixed as 0 (Zhang et al. 2016).

After determining the effective thickness of the sample at different temperatures, the $f_{LM}$ is then calculated from Eq. 2. In order to calculate $f_{LM}$, one needs to estimate the variation of the numerical density of resonant nuclei over the experimental time scale. We estimate the upper limit of the variation in numerical density of resonant nuclei using the data collected at the lowest and highest temperatures. At 1656 K and 54 GPa (ε-Fe), the calculated numerical density of resonant nuclei is 0.1779 mol/cm$^3$ (Fei et al., 2007). At 2842 K and 57 GPa (γ-Fe). the calculated numerical density of resonant nuclei is 0.1785 mol/cm$^3$ (Komabayashi et al., 2010). The estimated upper limit of the variations in numerical density during the experiment is 0.35%, much smaller than the experimental error. To simplify the calculation, we assume that the numerical density of resonant nuclei doesn't change during the experiment. By assuming that the sample chamber's thickness doesn't change during the experiment, as verified by X-ray absorption scans across the chamber before and after each heating cycle, the change of the physical thickness ($\Delta d$) is monitored using the ion chambers upstream and downstream from the sample:

$$\Delta d = \frac{A - A_0}{1/\mu_{\mathrm{KCl}} - 1/\mu_{\mathrm{Fe}}}, \quad (5)$$

where $\mu_{\mathrm{KCl}}$ and $\mu_{\mathrm{Fe}}$ are the attenuation lengths of KCl and Fe at 14.4125 keV (Henke et al. 1993), $A$ is the normalized X-ray absorption constrained from the ion chambers before and after the sample at each temperature, and $A_0$ is the normalized X-ray absorption before heating. The $f_{LM}$ at pressures ranging from around 50 to 60 GPa and a range of temperatures up to melting are listed in Tab. 1. We compare our results with previous NRIXS measurements on Fe (Shen et al. 2004; Lin et al. 2005; Mauger et al. 2014) at high pressures and temperatures (Fig. 3). We notice that the

267 $f_{LM}$ of $\gamma$- and $\epsilon$-Fe have the following features: within the experimental error, the temperature
268 dependence of the $f_{LM}$ of $\gamma$-Fe and $\epsilon$-Fe show a continuous linear trend up to melting and the effect
269 of temperature on the $f_{LM}$ is more significant than the effect of pressure. Using these features, we
270 build the following model (hereinafter referred to as the Lamb-Mössbauer factor with temperature
271 or FLMT model) to calculate the $f_{LM}$ of $\gamma$- and $\epsilon$-Fe at elevated P-T conditions. We assume that
272 the $f_{LM}$ of iron is a linear function of temperature between 300 K and the melting point at the
273 stability fields of $\gamma$- and $\epsilon$-Fe. At the melting point, the $f_{LM}$ of iron is fixed as zero (Jackson et al.
274 2013). So we have:
275
276 $$f_{LM}(T) = \frac{T_{melt}-T}{T_{melt}-300} f_{LM,300K}. \quad (6)$$
277
278 In Eq. (6), $T_{melt}$ is the melting temperature of iron at the experimental pressure (Zhang et al. 2016).
279 The $f_{LM}$ of $\epsilon$-Fe at 300 K is fitted as a function of pressure using an empirical equation (Murphy
280 et al. 2013): $f_{LM,300K}(P) = C - Ae^{-BP}$, where $A = 0.115(3)$, $B = 0.012(1)$ GPa$^{-1}$ and $C =$
281 $0.936(4)$. As is shown in Eq. (6), the FLMT model is not a linear-fit to the $f_{LM}$ data determined at
282 different experimental temperatures.
283
284 **3. From quasiharmonic Debye model to the equilibrium isotopic fractionation factor**
285
286 Under the harmonic approximation, a solid with N atoms has 3N-6 independent phonons. The
287 equations for the lattice vibrations can be solved exactly, and the $f_{LM}$ can be calculated for the
288 thermalized ensemble (Sturhahn and Jackson 2007; Murphy et al. 2013):
289

This is the peer-reviewed, final accepted version for American Mineralogist, published by the Mineralogical Society of America.
The published version is subject to change. Cite as Authors (Year) Title. American Mineralogist, in press.
DOI: https://doi.org/10.2138/am-2021-7884. http://www.minsocam.org/

290 $$f_{LM} = \exp[-\int \frac{E_R}{E} \coth(\frac{E}{2k_B T}) g(E) dE], \quad (7)$$

291

292 where $E_R$ is the recoil energy for the resonant nuclei (1.956 meV for $^{57}$Fe, Sturhahn and Jackson
293 2007), $E$ is the phonon energy and $g(E)$ is the partial (or projected) phonon DOS. The quantity
294 $g(E)$ is usually determined experimentally from an NRIXS spectrum (Sturhahn 2004). However,
295 with only the $f_{LM}$ available, it is not possible to determine the exact formulation of $g(E)$. When
296 the exact formulation of $g(E)$ is not known, one needs to prescribe a model for $g(E)$. We assume
297 weak anharmonicity which permits us to use a quasiharmonic model to describe the phonon
298 behavior of iron. In the Debye model, $g(E)$ has the following form (Debye 1913; Singwi and
299 Sjölander 1960; Leu and Sage 2016):

300

301 $$g(E) = \begin{cases} \frac{3E^2}{(k_B \theta_D)^3} & (E \leq k_B \theta_D), \\ 0 & (E > k_B \theta_D). \end{cases} \quad (8)$$

302

303 The parameter $\theta_D$ is the material-specific Debye temperature (Singwi and Sjölander 1960; Shen et
304 al. 2004; Leu and Sage 2016). $\theta_D$ varies with unit cell volume and is implicitly influenced by
305 temperature through thermal expansion in the quasiharmonic Debye model (Baroni et al. 2010;
306 Blanco et al. 2004). By combining Eqs. 1, 7 and 8 one can determine $\theta_D$ from $\langle u^2 \rangle$ with the
307 following relationship based on the Debye model (Singwi and Sjölander 1960; Shen et al. 2004):

308

309 $$-\frac{1}{k_0^2} \ln f_{LM} = \langle u^2 \rangle = \frac{6E_R}{k_0^2 k_B \theta_D} [\frac{1}{4} + (\frac{T}{\theta_D})^2 \int_0^{\frac{\theta_D}{T}} \frac{x}{e^x - 1} dx]. \quad (9)$$

310

311 As discussed in the introduction, the harmonic approximation doesn't have a volumetric
312 dependence of the lattice vibrational frequencies, and thus has shortcomings such as zero thermal
313 expansion, zero Grüneisen parameter and infinite lattice thermal conductivity (Erba 2014; Blanco
314 et al. 2004; Baroni et al. 2010). To overcome the drawbacks of the harmonic approximation, the
315 quasiharmonic approximation is often used to describe the behavior of real solids (Sturhahn and
316 Jackson 2007; Blanco et al. 2004; Mauger et al. 2014). The quasiharmonic approximation assumes
317 the existence of phonons (hence the use of Eq. 7 is justified), but does not consider phonon-phonon
318 interactions, and introduces an explicit dependence of vibration phonon frequencies on volume
319 (Erba 2014; Blanco et al. 2004; Mauger et al. 2014; Baroni et al. 2010; Wu 2010; Sturhahn and
320 Jackson 2007). The quasiharmonic approximation holds for many solids, while it fails for liquids
321 or fast atomic diffusion where the collective atomic motions are different from phonons (Sturhahn
322 and Jackson 2007). In the scope of this paper, the quasiharmonic Debye model is used.
323
324 The equilibrium isotopic fractionation $\beta$-factor is defined as the equilibrium isotopic fractionation
325 factor between a mineral phase that contains the element of interest X and the monatomic ideal
326 gaseous phase of element X (Richet et al. 1977; Schauble 2011; Huang et al. 2013; Eldridge et al.
327 2016). $\beta$-factor can be expanded as a function of the even powers of the inverse temperature $(1/T)$,
328 and the coefficients of each term is determined by the Debye temperature $\theta_D$ (Polyakov and
329 Mineev 2000; Polyakov et al. 2005). If one expands $\ln\beta$ to $1/T^6$, the equation is (Polyakov and
330 Mineev 2000; Polyakov et al. 2005; Dauphas et al. 2018):
331
332 $$\ln\beta_{I/I^*} = \left[\frac{3}{40}\left(\frac{\theta_D}{T}\right)^2 - \frac{1}{1120}\left(\frac{\theta_D}{T}\right)^4 + \frac{1}{60480}\left(\frac{\theta_D}{T}\right)^6\right] \times \left(\frac{M-M^*}{M^*}\right), \quad (10)$$
333

where $I$ and $I^*$ are two isotopes of masses $M$ and $M^*$, and $\theta_D$ is the Debye temperature calculated from Eq. 9. Using Eqs. 9 and 10, we calculate the equilibrium fractionation factor between $^{57}$Fe and $^{54}$Fe at different pressures and temperatures (Fig. 4). The $\beta$-factor between $^{57}$Fe and $^{54}$Fe of pure iron at room pressure is calculated using the $f_{LM}$ data of $\alpha$-iron up to the $\alpha - \gamma$ transition temperature from Mauger et al. (2014) (Fig. 4A). The $\beta$-factor of iron at ~50 GPa is calculated from our measured $f_{LM}$ data of $\gamma$- and $\epsilon$-Fe, and the $f_{LM}$ calculated from the 50 GPa FLMT model (Fig. 4B). At the melting point, $f_{LM}$ is zero and the value of $\langle u^2 \rangle$ in Eq. 9 diverges in the FLMT model.

Using a quasiharmonic Debye model, our data clearly shows that at high temperatures, the equilibrium isotopic fractionation $\ln\beta_{\mathrm{Fe}}^{57/54}$ is systematically lower than the results extrapolated from room temperature NRIXS data using the GM approach (Fig. 4), which is supported by published data (see Section 4). In several recent studies that utilized the GM approach, the $\ln\beta_{\mathrm{Fe}}^{57/54}$ was calculated from force constants that were derived from room temperature NRIXS spectra, and these force constants were assumed to be invariant with temperature (e.g., Dauphas et al. 2012; Shahar et al. 2016; Liu et al. 2017). Our calculation suggests that the quasiharmonic correction would systematically lower the $\ln\beta_{\mathrm{Fe}}^{57/54}$ between 1600 K and 2800 K at 50 GPa by ~0.1‰ when compared to the $\ln\beta_{\mathrm{Fe}}^{57/54}$ calculated at high temperature using a room temperature force constant, thus indicating the force constant varies with temperature.

## 4. Support of the quasiharmonic correction from published data

356 *4.1. Quasiharmonic correction of mantle and core materials constrained from macroscopic*
357 *thermodynamic quantities*
358
359 Polyakov (1998) and (2009) consider various temperature effects to the calculations of the isotope
360 fractionation $\beta$-factor, and suggest that intrinsic anharmonicity has a minor effect on the $\beta$-factor
361 (Polyakov 1998). Therefore, Polyakov (2009) evaluates the effects of temperature using the
362 approach of Gillet et al. (1996), but neglects the intrinsically anharmonic term (Polyakov 1998),
363 and provides an estimate to the quasiharmonic correction to the $\beta$-factor using the following
364 equation:
365
366 $$\frac{\Delta ln\beta}{ln\beta} = -\frac{6\gamma\gamma_{th}RT}{VK_T}, \quad (11)$$
367
368 where $\gamma$ is the normalized modal Grüneisen parameter, $\gamma_{th}$ is the thermal Grüneisen parameter
369 which is equal to $\gamma$ for single-element substances (e.g., Fe), $R$ is the gas constant, $V$ is the molar
370 volume and $K_T$ is the isothermal bulk modulus. Eq. (11) uses thermodynamic parameters that
371 cover the whole phonon spectrum, and is not limited by the Debye model where a cut-off phonon
372 energy exists (Polyakov 1998). Using updated thermodynamic parameters, we re-calculate the
373 quasiharmonic corrections to the $\beta$-factor of iron at high temperatures using Eq. 11. For $\alpha$-Fe at
374 1000 K and 1 bar, we use $\gamma$ = 1.81 (Mauger et al. 2014), $V$ = 7.32 cm$^3$/mol (Liu et al. 2004), and
375 $K_T$ = 139.1 GPa (Dever 1972). The estimated quasiharmonic correction of $\alpha$-Fe at 1000 K is -
376 0.12‰. For comparison, Polyakov (2009) estimated the upper bound of the quasiharmonic
377 correction to $\ln\beta_{\mathrm{Fe}}^{57/54}$ as ~-0.03‰ at 1000 K (1 bar) by assuming $V_{Fe}$ = 6.89 cm$^3$/mol and a
378 Grüneisen parameter $\gamma$ = 1.

379

380 For $\epsilon$-Fe at 50 GPa and 3000 K, we use $\gamma$ = 1.65 (Murphy et al. 2011), $V$ = 5.56 cm$^3$/mol (Murphy
381 et al. 2011), and $K_T$ = 240 GPa (Fei et al. 2016). The estimated quasiharmonic correction of $\epsilon$-Fe
382 at 50 GPa and 3000 K is -0.05‰. The Grüneisen parameters used in the re-calculation are
383 extrapolated from room temperature NRIXS results, and could introduce an estimated uncertainty
384 of up to 15% (estimated from the variation in Grüneisen parameters of $\epsilon$-Fe, Merkel et al. 2000;
385 Lubbers et al. 2000; Giefers et al. 2002; Murphy et al. 2011), which leads to a propagated
386 uncertainty of 0.02‰ to $\ln\beta_{\mathrm{Fe}}^{57/54}$ in the quasiharmonic correction. The quasiharmonic corrections
387 to $\ln\beta_{\mathrm{Fe}}^{57/54}$ of $\alpha$- and $\epsilon$-Fe using Eq. 11 are compatible with our estimations shown in Fig. 4 (-
388 0.10±0.02‰), and the quasiharmonic corrections constrained by both methods have consistent and
389 appropriate direction. One advantage of our approach is that the experiment is carried out in-situ
390 at high P-T conditions.

391

392 *4.2. Published data revisited: Does the general moments method capture the quasiharmonic*
393 *correction?*

394

395 The GM model can be derived either using the Bigeleisen-Mayer-Urey equation or using an
396 alternative approach from the kinetic energy (Bigeleisen and Mayer 1947; Urey 1947; Polyakov
397 1998, 2009; Dauphas et al. 2012). The Bigeleisen-Mayer-Urey equation is compatible with both
398 harmonic and quasiharmonic Debye models (Polyakov 1998) and is approximated by the GM
399 model using the phonon DOS when expanded in Taylor series (Kowalski and Jahn 2011). In order
400 for the GM model to be valid to approximate the Bigeleisen-Mayer-Urey equation, it is required

401 that the phonon angular frequencies $\omega$ ($cm^{-1}$) $< 8.73T$ (K) (Kowalski and Jahn 2011).[1] The
402 vibrational angular frequency of iron in minerals is usually less than 1000 $cm^{-1}$ (Dauphas et al.
403 2012), so the GM model can be used to calculate the $\beta$-factor at temperatures above 115 K.
404 Therefore, it is possible to validate the $\beta$-factor calculated from $f_{LM}$ with the GM model using
405 phonon DOS measurements at high temperatures.
406
407 We examined published DOS data that were collected at both room pressure and high pressures
408 from other research groups (Mauger et al. 2014; Lin et al. 2005). In the validation with the room
409 pressure data, we used the $f_{LM}$ and the phonon DOS that come from the same NRIXS dataset to
410 calculate the $\beta$-factor (Mauger et al. 2014). We calculated the $\beta$-factor from the $f_{LM}$ using Eqs. 9
411 and 10, and we calculated the $\beta$-factor from the high temperature phonon DOS using the equations
412 from the GM approach given in Polyakov (2009) and Dauphas et al. (2018). Fig. 5 demonstrates
413 that the $\beta$-factors calculated from the same high-temperature NRIXS data set using different
414 approaches are consistent with each other. Fig. 4A shows that the lnβ calculated from both the $f_{LM}$
415 (cyan squares, Fig. 4A) and the phonon DOS (magenta crosses, Fig. 4A) are lower than the
416 extrapolation of GM model using the phonon DOS collected at ambient temperature by about
417 0.1‰. Taken together, the results shown in Figs. 4 and 5 suggest that the $\beta$-factor computed from
418 NRIXS spectra collected at high temperatures and/or phonon DOS collected at high temperatures
419 leads to a more consistent result than the $\beta$-factor extrapolated to high temperatures using the force
420 constant derived from room temperature data.
421

[1] Kowalski and Jahn (2011) confused angular frequency $\omega$ with frequency $\nu$, and thus incorrectly assigned the condition as $\omega$ ($cm^{-1}$) $< 1.39T$ (K), which should be $\nu$ ($cm^{-1}$) $< 1.39T$ (K), or $\omega$ ($cm^{-1}$) $< 8.73T$ (K).

While most published high temperature $\beta$-factors calculated from the GM model were extrapolated from room temperature phonon DOS and/or force constants, Lin et al. (2005) measured the phonon DOS of ε-Fe at simultaneous high P-T conditions and reported the associated force constants, which are used to compare with the $\beta$-factors of ε-Fe determined by our approach. Fig. 6 demonstrates the lnβ of ε-Fe calculated from the GM method using force constants collected at simultaneous high P-T conditions (Lin et al. 2005) are at least 0.1‰ lower than the extrapolation of the GM model using a force constant collected at room temperature (54.6 GPa, 325.6 N/m, Dauphas et al. 2012), consistent with the quasiharmonic correction that we have observed with our approach. Our conclusion is that the GM method would capture the quasiharmonic corrections to the β-factor when the phonon DOS or force constants collected at high temperatures are used.

## 5. Discussion on the effect of phase transitions and pressure uncertainty

### *5.1. Phase transitions*

In this section we discuss reasons why the (lnβ, $10^6/T^2$) trend doesn't necessarily have to intercept the $10^6/T^2$ axis at (0, 0). The point (0, 0) in the (lnβ, $10^6/T^2$) space does not hold physical significance. The material presented in this study (solid Fe), and similar to all materials, is characterized by phase transitions with increasing temperature, and an intercept of (0, 0) from the extrapolation of the (lnβ, $10^6/T^2$) plot of the solid phase would neglect such phase transitions. Our results show that for the solid Fe phases, the (lnβ, $10^6/T^2$) trend does not intercept the (0, 0) point. Rather, the intercept of (lnβ, $10^6/T^2$) trend on the $10^6/T^2$ axis corresponds to a temperature higher than the melting point (see below), i.e., the solid phase never reaches it. For $T\rightarrow\infty$, a liquid will

turn into either a gas (below the critical pressure) or a supercritical state (above the critical pressure). The temperature dependence of lnβ in the high temperature phases (liquid, gas or supercritical) is generally unknown, except for a classical monatomic ideal gas (see below).

As Polyakov (1997) and Dauphas et al. (2018) have pointed out, lnβ is related to the average atomic kinetic energy (*KE*) based on the following equation:

$$ln\beta = \frac{\Delta m}{m^*}\left(\frac{KE}{k_B T} - \frac{3}{2}\right), \quad (12)$$

where $\Delta m$ is the mass difference between two isotopes, $m^*$ is the atomic mass of the element, and $k_B$ is the Boltzmann constant. In order for lnβ = 0, one only needs $KE = 3/2 k_B T$, which coincides with the average atomic kinetic energy of the classical monatomic ideal gas (Landau and Lifshitz, 1980). Therefore, the lnβ of a classical monatomic ideal gas is 0, which is the reason why the β-factor is defined as the isotope fractionation factor between the material of interest and a classical monatomic ideal gas reference (e.g., Richet et al. 1977; Schauble 2011; Huang et al. 2013; Eldridge et al. 2016).

Here we discuss two scenarios:

I): 1 bar. Fe has a sharp liquid-gas phase boundary and a well-defined gaseous phase at ambient pressure (boiling point 3273 K, Zhang et al. 2011). Evaporation experiments have demonstrated that Fe vapor behaves as a classical monatomic gas (Safarian and Engh, 2013). Based on the discussion above, we predict that lnβ of Fe would be equal to 0 at temperatures above its 1 bar

boiling point. To validate our prediction, we extrapolate (lnβ, $10^6/T^2$) of the data calculated from the $f_{LM}$ and DOS data from Mauger et al. (2014) to high temperatures using a linear model, and the linear extrapolations intercept the $10^6/T^2$ axis at temperatures of 3292 K ($f_{LM}$) and 4492 K (DOS) (please refer to the supplementary material). Both temperatures are above the 1 bar boiling point of Fe, but below infinity.

II): 50 GPa. The critical pressure of Fe is estimated at ~1 GPa (Ray et al. 2006), so Fe is unlikely to transition into a well-defined gaseous phase at 50 GPa. Instead Fe will likely go into the supercritical phase at high enough temperatures (Landau and Lifshitz, 1980). The linear extrapolation of (lnβ, $10^6/T^2$) derived from the $f_{LM}$ from our study intercepts the $10^6/T^2$ axis at a temperature of 3469 K. To our knowledge no study has constrained the supercritical transition temperature for Fe at 50 GPa, so it is challenging to benchmark this value. We expect that the harmonic model provides the highest possible bound for lnβ above the melting point of Fe, and the actual lnβ value is expected to be lower than the harmonic model (because the quasiharmonic correction would lower the lnβ, Fig. 4B).

### *5.2. Pressure uncertainty*

Murphy et al. (2013) determined the force constant of ε-Fe at ambient temperature and high pressures from the integrated phonon DOS. The pressure derivative of the force constant for ε-Fe is 2.124 N/(m·GPa), and the projected force constants at 50 GPa and 55 GPa are 293 N/m and 304 N/m, respectively. If we neglect the quasiharmonic correction and focus only on the intrinsic pressure effect, at 3000 K and 50 GPa, lnβ = 0.139‰; and at 3000 K and 55 GPa, lnβ = 0.144‰,

491 resulting in a $\Delta\ln\beta$ of 0.005‰. We carried out similar calculations with the force constant data
492 from Shahar et al. (2016) reported at 17 and 40 GPa, which is derived from the moments of the
493 refined NRIXS spectra. The pressure derivative of the force constant for ε-Fe from Shahar et al.
494 (2016) is 2.786 N/(m·GPa), resulting in a $\Delta\ln\beta$ of 0.007‰ between 50 GPa and 55 GPa at 3000 K.
495 The $\Delta\ln\beta$ that is intrinsically owing to the pressure effect (0.005‰ based on Murphy et al. 2013
496 or 0.007‰ based on Shahar et al. 2016) is more than one order of magnitude smaller than the
497 estimated quasiharmonic correction (0.1‰). The effect of the pressure uncertainty on the $\ln\beta$ is
498 therefore minor compared to the quasiharmonic correction at temperatures relevant to the core-
499 formation scenario, and the pressure uncertainty would not yield an intercept at (0, 0) for the ($\ln\beta$,
500 $10^6/T^2$) trend.
501
502 **6. Implications**
503
504 Our result demonstrates that the lattice vibrations of iron at high P-T conditions deviates from
505 harmonicity. One implication of our finding is to incorporate these results into studies involving
506 iron isotope fractionation, such as the core formation process. Geochemical studies have
507 demonstrated that mantle derived rocks are ~0.1‰ heavier in $\delta^{57}$Fe than rocks from Mars and
508 Vesta, which are believed to have chondritic $\delta^{57}$Fe value (Poitrasson et al. 2004; Sossi et al. 2016).
509 Based on NRIXS measurements, Polyakov (2009) suggests that the core-mantle differentiation
510 would leave an imprint on the iron isotope composition of the mantle rocks. However, based on
511 the harmonic extrapolation from recent high pressure, room temperature NRIXS measurements
512 where quasiharmonic correction is neglected, the isotope fractionation between metallic iron and

513 silicates at the core formation conditions (~40-60 GPa, ~3000 K) is expected to be smaller than
514 0.1‰.
515
516 Yang et al. (2019) determine the force constant of Fe in bridgmanite with a composition of
517 $Mg_{0.92}Fe_{0.09}Si_{0.99}O_3$ as 322.7±28.0 N/m at 50 GPa and 300 K, and the same group determine the
518 force constant of Fe in ferropericlase with a composition of $Mg_{0.75}Fe_{0.25}O$ as 333.1±17.6 N/m at
519 54 GPa and 300 K. If one neglects the quasiharmonic correction and calculates the high
520 temperature $\ln\beta_{Fe}^{57/54}$ from room temperature force constants, the $\ln\beta_{Fe}^{57/54}$ is 0.153±0.013‰ for
521 bridgmanite and 0.158±0.008‰ for ferropericlase at 3000 K. The force constant of Fe in ε-Fe
522 varies between different studies. If one takes an average of the force constants measured between
523 50 and 55 GPa from Lin et al. (2005) and Murphy et al. (2013), the averaged force constant in ε-
524 Fe is 309±11 N/m at 53 GPa and 300 K, which corresponds to a $\ln\beta_{Fe}^{57/54}$ of 0.147±0.005‰ at
525 3000 K without a quasiharmonic correction. If the quasiharmonic correction is neglected, the
526 difference in $\ln\beta_{Fe}^{57/54}$ between Fe and mantle materials at ~50 GPa and 3000 K is in the order of
527 0.01‰. We now compare with previous studies that did not consider a quasiharmonic correction
528 and find that they led to similar results. Using phonon DOS calculated from density functional
529 theory, Shahar et al. (2016) calculate the iron isotopic fractionation between bridgmanite and iron
530 ($\Delta^{57}Fe_{Brg\text{-}Fe} = \delta^{57}Fe_{Brg} - \delta^{57}Fe_{Fe} = \ln\beta_{Brg}^{57/54}Fe - \ln\beta_{Fe}^{57/54}Fe$) at 60 GPa and ~3500 K as 0.02-
531 0.04‰. Using basaltic glass as a proxy for mantle minerals, Liu et al. (2017) calculate
532 $\Delta^{56}Fe_{mantle\text{-}Fe}$ at 40-60 GPa and 3000-4000 K as 0-0.02‰, which is equivalent to a $\Delta^{57}Fe_{mantle\text{-}Fe}$
533 of 0-0.03‰ if one recalculates the $\delta^{57}Fe$ using the same force constant as $\delta^{56}Fe$. Both studies
534 conclude that the core formation process is unlikely to leave an iron isotopic fingerprint on mantle

535 rocks. However, if quasiharmonic correction is considered, there may be an observable effect as
536 discussed below.
537
538 We now consider rough estimates of the quasiharmonic correction to the $\beta$-factor of lower mantle
539 minerals using Eq. 11. Wolf et al. (2015) measured the thermal equation of state of iron-bearing
540 bridgmanite and thus provide constraints on all the parameters in Eq. 11; in this case, one needs to
541 assume that the normalized modal Grüneisen parameter $\gamma$ of iron in bridgmanite is the same as its
542 thermal Grüneisen parameter, which is yet to be tested. At 50 GPa and 3000 K, the thermal
543 Grüneisen parameter $\gamma_{th}$ for iron-bearing bridgmanite is 1.3, the isothermal bulk modulus is 370.6
544 GPa, and molar volume is 24.6 $cm^3$/mol (Wolf et al. 2015). Using Eq. 11, the estimated
545 quasiharmonic correction to $\ln\beta_{\mathrm{Fe}}^{57/54}$ in bridgmanite is -0.006‰. If we now use this estimated
546 quasiharmonic correction to $\beta$-factors in bridgmanite and the quasiharmonic correction in metallic
547 iron determined from this study (-0.1‰), the core formation process, modeled as $\Delta^{57}\mathrm{Fe}_{\mathrm{Brg\text{-}Fe}}$,
548 would leave an isotopic fingerprint of 0.09-0.13‰. This $\Delta^{57}\mathrm{Fe}_{\mathrm{Brg\text{-}Fe}}$ value is close to the $\delta^{57}$Fe
549 compared between mantle-derived rocks and chondrites (~0.1‰) (Poitrasson et al. 2004; Wang et
550 al. 2012; Sossi et al. 2016). For ferropericlase, the other major Fe-bearing major phase in the lower
551 mantle, the reported thermoelastic parameters at 50 GPa and 3000 K are: $V$ = 10.4 $cm^3$/mol (Mao
552 et al. 2011), $K_T$ = 292.0 GPa (Mao et al. 2011), and $\gamma$ = 1.3 (Fischer et al. 2011). Based on Eq. 11,
553 the estimated quasiharmonic correction to $\ln\beta_{\mathrm{Fe}}^{57/54}$ in ferropericlase is -0.013‰, which is also
554 significantly smaller than that for the metallic Fe phase (-0.1‰) and will not change the conclusion
555 that $^{57}$Fe preferentially partitions into these lower mantle phases when considering the
556 quasiharmonic correction.
557

558 The exact fraction of the equilibrium $\delta^{57}$Fe that would be transferred to the mantle depends on the
559 mass ratio of iron between the metallic phase and the mantle phases in the core-formation process.
560 If we assume that 90% of the iron is in the core, based on the lever rule ($\delta^{57}Fe_{mantle} = (\delta^{57}Fe_{Earth}$-
561 $\delta^{57}Fe_{core}f^{Fe}_{core})/(1-f^{Fe}_{core})$; $\delta^{57}Fe_{mantle} - \delta^{57}Fe_{core} = 0.1‰$) the calculated $\delta^{57}Fe_{mantle}$ is 0.09‰. This
562 $\delta^{57}Fe_{mantle}$ value is close to the $\delta^{57}$Fe compared between mantle-derived rocks and chondrites
563 (~0.1‰) (Poitrasson et al. 2004; Wang et al. 2012; Sossi et al. 2016). Our conclusion is that one
564 cannot rule out the possibility that the core formation process would leave the mantle enriched
565 with heavier iron isotopes compared to chondrites (Poitrasson et al. 2004; Weyer et al. 2005;
566 Schoenberg and Blanckenburg 2006).
567
568 **7. Conclusions**
569
570 We constrain the mean-square displacement of the iron atoms by measuring the $f_{LM}$ of $\gamma$- and $\epsilon$-
571 Fe at pressures around 50 GPa and temperatures above 1650 K using synchrotron Mössbauer
572 spectroscopy. This approach avoids the difficulty in maintaining stable and uniform high sample
573 temperatures for hours, a requirement in conventional Mössbauer and NRIXS measurements.
574 Extrapolation of our results to 300-1700 K, where previous measurements have been conducted,
575 show good agreement, suggesting that the $f_{LM}$ captures the behavior of the phonons in iron metal
576 reasonably well.
577
578 We find that the $f_{LM}$ is more sensitive to temperature than to pressure, and the temperature
579 dependence for $\gamma$ - and $\epsilon$ -Fe varies continuously up to melting, within the experimental

uncertainties. At the pressures investigated here (around 50 GPa), the $f_{LM}$ of iron has a linear temperature dependence.

We establish the relationship between $f_{LM}$, the lattice vibrations of iron and iron isotope fractionation. We assume weak anharmonicity which permits us to use a quasiharmonic Debye model for the lattice vibrations. We calculate the Debye temperatures of the $\gamma$- and $\epsilon$-Fe at elevated pressure-temperature conditions from this model. From the calculated Debye temperatures, the equilibrium isotopic fractionation $\beta$-factors of iron at high pressures and high temperatures is computed. Our result is consistent with the $\beta$-factors determined by previous NRIXS studies at relatively low temperature ($T < 600$ K). However, for the high temperature data ($T > 600$ K), we find that the quasiharmonic correction is significant enough to have an observable isotopic effect. Calculations based on our experimental data (around 50 GPa, 1600-2800 K) demonstrate that the quasiharmonic correction would lower $\ln\beta_{\mathrm{Fe}}^{57/54}$ by 0.1‰ compared to the extrapolation of room temperature NRIXS results. The offset of 0.1‰ in $\ln\beta_{\mathrm{Fe}}^{57/54}$ is enough to account for the observed $\delta^{57}$Fe in mantle rocks compared to chondrites. Therefore, it is plausible that core formation processes left an observable iron isotopic signature in mantle rocks. Our experimental results on hot compressed iron highlight the importance of considering nonharmonic effects to the evaluation of isotopic fractionation $\beta$-factors in minerals at deep earth conditions.

## Acknowledgements

The authors thank Dr. Thomas S. Toellner for his help with the experiments. We thank the National Science Foundation (EAR-CSEDI-1316362, EAR-CSEDI-2009935 and EAR-1727020) for support of this research.

Use of the Advanced Photon Source is supported by the Department of Energy, Office of Science (DE-AC02-06CH11357). Sector 3 operations are supported in part by COMPRES under National Science Foundation Cooperative Agreement EAR-1661511. We thank GeoSoilEnviroCARS (NSF EAR-1634415 and DOE DE-FG02-94ER14466) for the help with sample preparation. D.Z. acknowledges the Argonne Graduate Research Program to support part of this research. We also thank Dr. Lisa Mauger for kindly providing the published phonon DOS of $\alpha$-Fe from her paper. The authors acknowledge Dr. Veniamin B. Polyakov, Dr. Aleksandr Chumakov and Dr. Paolo Sossi for their thoughtful, thorough and constructive comments, which helped to improve our manuscript.

## References

Alfè, D., Gillan, M., Price, G., 1999. The melting curve of iron at the pressures of the earth's core from ab initio calculations. Nature 401 (6752), 462–464.

Alfè, D., Gillan, M. J., Price, G. D., 2002. Composition and temperature of the Earth's core constrained by combining ab initio calculations and seismic data. Earth and Planetary Science Letters 195 (1-2), 91–98.

Alfè, D., Voc adlo, L., Price, G. D., Gillan, M. J., 2004. Melting curve of materials: theory versus experiments. Journal of Physics: Condensed Matter 16 (14), S973–S982.

Allen, P. B., 2020. Theory of thermal expansion: Quasi-harmonic approximation and corrections from quasi-particle renormalization. Modern Physics Letters B 34 (02), 2050025.

Bansal, D., Aref, A., Dargush, G., Delaire, O., jul 2016. Modeling non-harmonic behavior of materials from experimental inelastic neutron scattering and thermal expansion measurements. Journal of Physics: Condensed Matter 28 (38), 385201.

626 Baroni, S., Giannozzi, P., Isaev, E., 2010. Density-functional perturbation theory for quasi-
627 harmonic calculations. Reviews in Mineralogy and Geochemistry 71 (1), 39.
628 Bergmann, U., Shastri, S. D., Siddons, D. P., Batterman, B. W., Hastings, J. B., 1994.
629 Temperature dependence of nuclear forward scattering of synchrotron radiation in α-$^{57}$Fe.
630 Physical Review B 50, 5957–5961.
631 Bigeleisen, J., Mayer, M. G., 1947. Calculation of equilibrium constants for isotopic exchange
632 reactions. The Journal of Chemical Physics 15 (5), 261–267.
633 Blanco, M., Francisco, E., LuaÃ±a, V., 2004. Gibbs: isothermal-isobaric thermodynamics of
634 solids from energy curves using a quasi-harmonic debye model. Computer Physics
635 Communications 158 (1), 57 – 72.
636 Boyle, A. J. F., Bunbury, D. S. P., Edwards, C., Hall, H. E., 1961. The Mössbauer effect in tin
637 from 120 K to the melting point. Proceedings of the Physical Society 77 (1), 129.
638 Brown, J. S., 1969. Anharmonic effects on the Mössbauer recoilless fraction of solid krypton.
639 Physical Review 187, 401–402.
640 Chai, M., Brown, J. M., Slutsky, L. J., Oct 1996. Thermal diffusivity of mantle minerals. Physics
641 and Chemistry of Minerals 23 (7), 470–475.
642 Chen, B., Li, Z., Zhang, D., Liu, J., Hu, M. Y., Zhao, J., Bi, W., Alp, E. E., Xiao, Y., Chow, P.,
643 Li, J., 2014. Hidden carbon in Earth's inner core revealed by shear softening in dense $Fe_7C_3$.
644 Proceedings of the National Academy of Sciences 111 (50), 17755–17758.
645 Chumakov, A. I., Rüffer, R., Baron, A. Q. R., Grünsteudel, H., Grünsteudel, H. F., 1996.
646 Temperature dependence of nuclear inelastic absorption of synchrotron radiation in α-
647 $^{57}Fe$. Physical Review B 54, R9596–R9599.

Chumakov, A. I., Sturhahn, W., 1999. Experimental aspects of inelastic nuclear resonance scattering. Hyperfine Interactions 123-124 (1-4), 781–808.

Dauphas, N., Hu, M. Y., Baker, E. M., Hu, J., Tissot, F. L. H., Alp, E. E., Roskosz, M., Zhao, J., Bi, W., Liu, J., Lin, J.-F., Nie, N. X., Heard, A., Sep 2018. *SciPhon*: a data analysis software for nuclear resonant inelastic X-ray scattering with applications to Fe, Kr, Sn, Eu and Dy. Journal of Synchrotron Radiation 25 (5), 1581–1599.

Dauphas, N., Roskosz, M., Alp, E. E., Golden, D. C., Sio, C. K., Tissot, F. L. H., Hu, M. Y., Zhao, J., Gao, L., Morris, R. V., 2012. A general moment NRIXS approach to the determination of equilibrium Fe isotopic fractionation factors: Application to goethite and jarosite. Geochimica et Cosmochimica Acta 94, 254–275.

Debye, P., 1913. Uber die intensitatsverteilung in den mit rontgenstrahlen erzeugten interferenzbildern. Verhandlungen der Deutschen Physikalischen Gesellschaft 15, 738-752.

Dever, D., 1972. Temperature dependence of the elastic constants in α- iron single crystals: relationship to spin order and diffusion anomalies. Journal of Applied Physics 43 (8), 3293–3301.

Dunitz, J. D., Schomaker, V., Trueblood, K. N., 1988. Interpretation of atomic displacement parameters from diffraction studies of crystals. The Journal of Physical Chemistry 92 (4), 856–867.

Eldridge, D. L., Guo, W., Farquhar, J., 2016. Theoretical estimates of equilibrium sulfur isotope effects in aqueous sulfur systems: Highlighting the role of isomers in the sulfite and sulfoxylate systems. Geochimica et Cosmochimica Acta 195, 171 – 200.

Erba, A., 2014. On combining temperature and pressure effects on structural properties of crystals with standard ab initio techniques. The Journal of Chemical Physics 141 (12), 124115.

Fei, Y., Murphy, C., Shibazaki, Y., Shahar, A., Huang, H., 2016. Thermal equation of state of hcp-iron: Constraint on the density deficit of earth's solid inner core. Geophysical Research Letters 43 (13), 6837–6843.

Fischer, R. A., Campbell, A. J., Shofner, G. A., Lord, O. T., Dera, P., Prakapenka, V. B., 2011. Equation of state and phase diagram of feo. Earth and Planetary Science Letters 304 (3), 496 – 502.

Fultz, B., 2010. Vibrational thermodynamics of materials. Progress in Materials Science 55 (4), 247 – 352.

Giefers, H., R. Lübbers, K. Rupprecht, G. Wortmann, D. Alfè, and A. I. Chumakov, 2002. Phonon spectroscopy of oriented hcp iron, High Pressure Res., 22(2), 501–506.

Gillet, P., McMillan, P., Schott, J., Badro, J., Grzechnik, A., 1996. Thermodynamic properties and isotopic fractionation of calcite from vibrational spectroscopy of 18o-substituted calcite. Geochimica et Cosmochimica Acta 60 (18), 3471 – 3485.

Henke, B. L., Gullikson, E. M., Davis, J. C., 1993. X-ray interactions: photoabsorption, scattering, transmission, and reflection at E=50-30000 eV, Z=1-92. Atomic Data and Nuclear Data Tables 54 (2), 181–342.

Huang, F., Chen, L., Wu, Z., Wang, W., 2013. First-principles calculations of equilibrium mg isotope fractionations between garnet, clinopyroxene, orthopyroxene, and olivine: Implications for mg isotope thermometry. Earth and Planetary Science Letters 367, 61 – 70.

693 Jackson, J. M., Sturhahn, W., Lerche, M., Zhao, J., Toellner, T. S., Alp, E. E., Sinogeikin, S. V.,
694 Bass, J. D., Murphy, C. A., Wicks, J. K., 2013. Melting of compressed iron by
695 monitoring atomic dynamics. Earth and Planetary Science Letters 362, 143–150.
696 Jeanloz, R., Morris, S., 1986. Temperature distribution in the crust and mantle. Annual Review
697 of Earth and Planetary Sciences 14 (1), 377–415.
698 Jeanloz, R., Richter, F. M., 1979. Convection, composition, and the thermal state of the lower
699 mantle. Journal of Geophysical Research: Solid Earth 84 (B10), 5497–5504.
700 Kieffer, S. W., 1979a. Thermodynamics and lattice vibrations of minerals: 1. mineral heat
701 capacities and their relationships to simple lattice vibrational models. Reviews of
702 Geophysics 17 (1), 1–19.
703 Kieffer, S. W., 1979b. Thermodynamics and lattice vibrations of minerals: 2. vibrational
704 characteristics of silicates. Reviews of Geophysics 17 (1), 20–34.
705 Kieffer, S. W., 1979c. Thermodynamics and lattice vibrations of minerals: 3. lattice dynamics
706 and an approximation for minerals with application to simple substances and framework
707 silicates. Reviews of Geophysics 17 (1), 35–59.
708 Kieffer, S. W., 1980. Thermodynamics and lattice vibrations of minerals: 4. application to chain
709 and sheet silicates and orthosilicates. Reviews of Geophysics 18 (4), 862–886.
710 Kieffer, S. W., 1982. Thermodynamics and lattice vibrations of minerals: 5. applications to phase
711 equilibria, isotopic fractionation, and high-pressure thermodynamic properties. Reviews
712 of Geophysics 20 (4), 827–849.
713 Kim, D. S., Hellman, O., Herriman, J., Smith, H. L., Lin, J. Y. Y., Shulumba, N., Niedziela, J. L.,
714 Li, C. W., Abernathy, D. L., Fultz, B., 2018. Nuclear quantum effect with pure

715 anharmonicity and the anomalous thermal expansion of silicon. Proceedings of the
716 National Academy of Sciences 115 (9), 1992–1997.
717 Kolk, B., Bleloch, A. L., Hall, D. B., 1986. Recoilless fraction studies of iron near the curie
718 temperature. Hyperfine Interactions 29 (1-4), 1377–1380.
719 Komabayashi, T., Fei, Y., Meng, Y., Prakapenka, V. B., 2009. In-situ x-ray diffraction
720 measurements of the γ−ε transition boundary of iron in an internally-heated diamond
721 anvil cell. Earth and Planetary Science Letters 282
722 Komabayashi, T., and Fei, Y. 2010. Internally consistent thermodynamic database for iron to the
723 Earth's core conditions, J. Geophys. Res., 115(1-4), 252–257.
724 Kovats, T. A., Walker, J. C., 1969. Mössbauer absorption in $Fe^{57}$ in metallic iron from the curie
725 point to the γ-δ transition. Physical Review 181, 610–618.
726 Kowalski, P. M., Jahn, S., 2011. Prediction of equilibrium li isotope fractionation between
727 minerals and aqueous solutions at high p and t: An efficient ab initio approach.
728 Geochimica et Cosmochimica Acta 75 (20), 6112 – 6123.
729 Landau, L., Lifshitz, E., 1980. Statistical Physics: Part I. No. Third Edition. Pergamon.
730 Leu, B. M., Sage, J. T., 2016. Stiffness, resilience, compressibility. Hyperfine Interactions
731 237 (1), 87.
732 Lin, J.-F., Sturhahn, W., Zhao, J., Shen, G., Mao, H.-K., Hemley, R. J., 2005. Sound velocities of
733 hot dense iron: Birch's law revisited. Science 308 (5730), 1892–1894.
734 Liu, J., Dauphas, N., Roskosz, M., Hu, M. Y., Yang, H., Bi, W., Zhao, J., Alp, E. E., Hu, J. Y.,
735 Lin, J.-F., 2017. Iron isotopic fractionation between silicate mantle and metallic core at
736 high pressure. Nature Communications 8, 14377.

737 Liu, Y., Sommer, F., Mittemeijer, E., 2004. Calibration of the differential dilatometric
738 measurement signal upon heating and cooling; thermal expansion of pure iron.
739 Thermochimica Acta 413 (1), 215 – 225.
740 Lübbers, R., H. F. Grünsteudel, A. I. Chumakov, and G. Wortmann, 2000, Density of phonon
741 states in iron at high pressure, Science, 287(5456), 1250–1253.
742 Macedo, W. A. A., Keune, W., 1988. Magnetism of epitaxial fcc-Fe(100) films on Cu(100)
743 investigated in situ by conversion-electron Mössbauer spectroscopy in ultrahigh vacuum.
744 Physical Review Letters 61, 475–478.
745 Mao, Z., Lin, J.-F., Liu, J., Prakapenka, V. B., 2011. Thermal equation of state of lower-mantle
746 ferropericlase across the spin crossover. Geophysical Research Letters 38 (23).
747 Mauger, L., Lucas, M. S., Muñoz, J. A., Tracy, S. J., Kresch, M., Xiao, Y., Chow, P., Fultz, B.,
748 2014. Nonharmonic phonons in α-iron at high temperatures. Physical Review B 90,
749 064303.
750 Merkel, S., A. F. Goncharov, H. K. Mao, P. Gillet, and R. J. Hemley 2000, Raman spectroscopy
751 of iron to 152 gigapascals: Implications for Earth's inner core, Science, 288(5471), 1626–
752 1629.
753 Morrison, R. A., Jackson, J. M., Sturhahn, W., Zhao, J., Toellner, T. S., 2019. High pressure
754 thermoelasticity and sound velocities of fe-ni-si alloys. Physics of the Earth and Planetary
755 Interiors 294, 106268.
756 Murphy, C. A., Jackson, J. M., Sturhahn, W., 2013. Experimental constraints on the
757 thermodynamics and sound velocities of hcp-Fe to core pressures. Journal of Geophysical
758 Research: Solid Earth 118 (5), 1999–2016.

759 Murphy, C. A., Jackson, J. M., Sturhahn, W., Chen, B., 2011. Grüneisen parameter of hcp-Fe to
760 171 GPa. Geophysical Research Letters 38 (24), L24306.
761 Oganov, A., Brodholt, J. P., Price, G. D., 2000. Comparative study of quasiharmonic lattice
762 dynamics, molecular dynamics and Debye model applied to $MgSiO_3$ perovskite. Physics
763 of the Earth and Planetary Interiors 122, 277–288.
764 Poitrasson, F., Halliday, A. N., Lee, D.-C., Levasseur, S., Teutsch, N., 2004. Iron isotope
765 differences between earth, moon, mars and vesta as possible records of contrasted
766 accretion mechanisms. Earth and Planetary Science Letters 223 (3), 253 – 266.
767 Polyakov, V., Mineev, S., Clayton, R., Hu, G., Gurevich, V., Khramov, D., Gavrichev, K.,
768 Gorbunov, V., Golushina, L., 2005. Oxygen isotope fractionation factors involving
769 cassiterite (sno2): I. calculation of reduced partition function ratios from heat capacity
770 and x-ray resonant studies. Geochimica et Cosmochimica Acta 69 (5), 1287 – 1300.
771 Polyakov, V. B., 1997. Equilibrium fractionation of the iron isotopes: Estimation from
772 mössbauer spectroscopy data. Geochimica et Cosmochimica Acta 61 (19), 4213 – 4217.
773 Polyakov, V. B., 1998. On anharmonic and pressure corrections to the equilibrium isotopic
774 constants for minerals. Geochimica et Cosmochimica Acta 62 (18), 3077–3085.
775 Polyakov, V. B., 2009. Equilibrium iron isotope fractionation at core-mantle boundary
776 conditions. Science 323 (5916), 912–914.
777 Polyakov, V. B., Clayton, R. N., Horita, J., Mineev, S. D., 2007. Equilibrium iron isotope
778 fractionation factors of minerals: Reevaluation from the data of nuclear inelastic resonant
779 X-ray scattering and Mössbauer spectroscopy. Geochimica Et Cosmochimica Acta
780 71 (15), 3833–3846.

781 Polyakov, V. B., Mineev, S. D., 2000. The use of mössbauer spectroscopy in stable isotope
782 geochemistry. Geochimica et Cosmochimica Acta 64 (5), 849 – 865.
783 Prescher, C., Prakapenka, V. B., 2015. DIOPTAS: a program for reduction of two-dimensional
784 X-ray diffraction data and data exploration. High Pressure Research 35 (3), 223–230.
785 Ray, A., Srivastava, M., Kondayya, G., Menon, S., 2006. Improved equation of state of metals in
786 the liquid-vapor region. Laser and Particle Beams 24 (3), 437–445.
787 Reynard, B., Caracas, R., McMillan, P., 2015. Lattice vibrations and spectroscopy of mantle
788 phases. In: Schubert, G. (Ed.), Treatise on Geophysics (Second Edition), second edition
789 Edition. Elsevier, Oxford, pp. 203 – 231.
790 Richet, P., Bottinga, Y., Javoy, M., 1977. A review of hydrogen, carbon, nitrogen, oxygen,
791 sulphur, and chlorine stable isotope fractionation among gaseous molecules. Annual
792 Review of Earth and Planetary Sciences 5 (1), 65–110.
793 Rothchild, E., Li, Q., Ma, E., 2019. On the validity of using the Debye model to quantitatively
794 correlate the shear modulus with vibrational properties in cubic metals. Scripta Materialia
795 158, 34–37.
796 Safarian, J., Engh, T. A., 2013. Vacuum evaporation of pure metals. Metallurgical and Materials
797 Transactions A 44 (2), 747–753.
798 Schauble, E. A., 2011. First-principles estimates of equilibrium magnesium isotope fractionation
799 in silicate, oxide, carbonate and hexaaquamagnesium(2+) crystals. Geochimica et
800 Cosmochimica Acta 75 (3), 844 – 869.
801 Schoenberg, R., von Blanckenburg, F., 2006. Modes of planetary-scale fe isotope fractionation.
802 Earth and Planetary Science Letters 252 (3), 342 – 359.

803 Shahar, A., Schauble, E. A., Caracas, R., Gleason, A. E., Reagan, M. M., Xiao, Y., Shu, J., Mao,
804 W., 2016. Pressure-dependent isotopic composition of iron alloys. Science 352 (6285),
805 580–582.
806 Shen, G., Heinz, D. L., 1998. High-pressure melting of deep mantle and core materials. Reviews
807 in Mineralogy and Geochemistry 37 (1), 369.
808 Shen, G., Sturhahn, W., Alp, E. E., Zhao, J., Tollenner, T. S., Prakapenka, V. B., Meng, Y., Mao,
809 H.-K., 2004. Phonon density of states in iron at high pressures and high temperatures.
810 Physics and Chemistry of Minerals 31 (6), 353–359.
811 Singwi, K. S., Sjölander, A., 1960. Resonance absorption of nuclear gamma rays and the
812 dynamics of atomic motions. Physical Review 120, 1093–1102.
813 Sossi, P. A., Nebel, O., Anand, M., Poitrasson, F., 2016. On the iron isotope composition of mars
814 and volatile depletion in the terrestrial planets. Earth and Planetary Science Letters 449,
815 360 – 371.
816 Sturhahn, W., 1999. Phase problem in synchrotron Mössbauer spectroscopy. Physical Review B
817 63, 094105.
818 Sturhahn, W., 2000. CONUSS and PHOENIX: Evaluation of nuclear resonant scattering data.
819 Hyperfine Interactions 125 (1-4), 149–172.
820 Sturhahn, W., 2004. Nuclear resonant spectroscopy. Journal of Physics-Condensed Matter
821 16 (5), S497–S530.
822 Sturhahn, W., 2020. MINeral physics UTIlity (MINUTI) open-source software package.
823 www.nrixs.com
824 Sturhahn, W., Chumakov, A., Mar 1999. Lamb–mössbauer factor and second-order doppler shift
825 from inelastic nuclear resonant absorption. Hyperfine Interactions 123 (1), 809–824.

826 Sturhahn, W., Jackson, J. M., 2007. Geophysical applications of nuclear resonant scattering. In:
827 Advances in High-Pressure Mineralogy: GSA Special Paper 421. Geological Society of
828 America, Boulder, Colorado, pp. 157–174.
829 Toellner, T. S., 2000. Monochromatization of synchrotron radiation for nuclear resonant
830 scattering experiments. Hyperfine Interactions 125 (1-4), 3–28.
831 Trueblood, K. N., Bürgi, H.-B., Burzlaff, H., Dunitz, J. D., Gramaccioli, C. M., Schulz, H. H.,
832 Shmueli, U., Abrahams, S. C., Sep 1996. Atomic Dispacement Parameter Nomenclature.
833 Report of a Subcommittee on Atomic Displacement Parameter Nomenclature. Acta
834 Crystallographica Section A 52 (5), 770–781.
835 Tse, J., Klug, D., Zhao, J., Sturhahn, W., Alp, E., Baumert, J., Gutt, C., Johnson, M., Press, W.,
836 2005. Anharmonic motions of kr in the clathrate hydrate. Nature Materials 4 (12), 917.
837 Urey, H. C., 1947. The thermodynamic properties of isotopic substances. J. Chem. Soc., 562–
838 581.
839 Vočadlo, L., Alfe, D., 2002. Ab initio melting curve of the fcc phase of aluminum. Physical
840 Review B 65 (21), 214105.
841 Wang, K., Moynier, F., Dauphas, N., Barrat, J.-A., Craddock, P., Sio, C. K., 2012. Iron isotope
842 fractionation in planetary crusts. Geochimica et Cosmochimica Acta 89, 31 – 45.
843 Wentzcovitch, R. M., Yu, Y. G., Wu, Z., 2010. Thermodynamic properties and phase relations in
844 mantle minerals investigated by first principles quasiharmonic theory. Reviews in
845 Mineralogy and Geochemistry 71 (1), 59.
846 Weyer, S., Anbar, A. D., Brey, G. P., Munker, C., Mezger, K., Woodland, A. B., 2005. Iron
847 isotope fractionation during planetary differentiation. Earth and Planetary Science Letters
848 240 (2), 251 – 264.

Wicks, J. K., Jackson, J. M., Sturhahn, W., Zhang, D., 2017. Sound velocity and density of magnesiowüstites: Implications for ultralow-velocity zone topography. Geophysical Research Letters 44 (5), 2148–2158.

Wolf, A. S., Jackson, J. M., Dera, P., Prakapenka, V. B., 2015. The thermal equation of state of (mg, fe)sio3 bridgmanite (perovskite) and implications for lower mantle structures. Journal of Geophysical Research: Solid Earth 120 (11), 7460–7489.

Wu, Z., May 2010. Calculating the anharmonic free energy from first principles. Phys. Rev. B 81, 172301.

Yang, H., Lin, J.F., Hu, M.Y., Roskosz, M., Bi, W., Zhao, J., Alp, E.E., Liu, J., Liu, J., Wentzcovitch, R.M. Okuchi, T., 2019. Iron isotopic fractionation in mineral phases from Earth's lower mantle: Did terrestrial magma ocean crystallization fractionate iron isotopes? Earth and Planetary Science Letters 506, 113-122.

Young, E. D., Galy, A., Nagahara, H., 2002. Kinetic and equilibrium mass-dependent isotope fractionation laws in nature and their geochemical and cosmochemical significance. Geochimica et Cosmochimica Acta 66 (6), 1095 – 1104.

Yu, Y. G., Wentzcovitch, R. M., Angel, R. J., 2010. First principles study of thermodynamics and phase transition in low-pressure ($P2_1/c$) and high-pressure (C2/c) clinoenstatite $MgSiO_3$. Journal of Geophysical Research: Solid Earth 115 (B2), B02201.

Yu, Y. G., Wu, Z., Wentzcovitch, R. M., 2008. $\alpha-\beta-\gamma$ transformations in $Mg_2SiO_4$ in Earth's transition zone. Earth and Planetary Science Letters 273 (1), 115 – 122.

Zhang, D., Jackson, J. M., Chen, B., Sturhahn, W., Zhao, J., Yan, J., Caracas, R., 2013. Elasticity and lattice dynamics of enstatite at high pressure. Journal of Geophysical Research: Solid Earth 118 (8), 4071–4082.

Zhang, D., Jackson, J. M., Zhao, J., Sturhahn, W., Alp, E. E., Hu, M. Y., Toellner, T. S., Murphy, C. A., Prakapenka, V. B., 2016. Temperature of Earth's core constrained from melting of Fe and $Fe_{0.9}Ni_{0.1}$ at high pressures . Earth and Planetary Science Letters 447, 72–83.

Zhang, D., Jackson, J. M., Zhao, J., Sturhahn, W., Alp, E. E.and Toellner, T. S., Hu, M. Y., 2015. Fast temperature spectrometer for samples under extreme conditions. Review of Scientific Instruments 86 (1), 013105.

Zhang, Y., Evans, J. R. G., Yang, S., 2011. Corrected values for boiling points and enthalpies of vaporization of elements in handbooks. Journal of Chemical & Engineering Data 56 (2), 328–337.

**Table 1.** Lamb-Mössbauer factor and β-factor of iron at various temperatures and pressures determined in this study. Numbers in parentheses indicate the errorbar rounded to the last significant digit. At the melting point the β-factor is not available due to the divergence when calculating $\langle u^2 \rangle$ using Eq. 1.

| **Run1** | | | | **Run2** | | | |
|---|---|---|---|---|---|---|---|
| T (K) | P (GPa) | $f_{LM}$ | $\ln\beta_{57/54}$ (‰) | T (K) | P (GPa) | $f_{LM}$ | $\ln\beta_{57/54}$ (‰) |
| 1656(61) | 54(3) | 0.41(9) | 0.38(8) | 1675(53) | 51(4) | 0.41(6) | 0.37(6) |
| 1957(78) | 55(3) | 0.38(8) | 0.29(6) | 1740(60) | 51(4) | 0.43(7) | 0.38(7) |
| 2107(42) | 56(3) | 0.30(8) | 0.22(5) | 1988(88) | 53(4) | 0.28(3) | 0.22(2) |

| | | | | | | | |
|---|---|---|---|---|---|---|---|
| 2330(51) | 57(3) | 0.24(3) | 0.17(1) | 2173(35) | 54(4) | 0.183(7) | 0.151(3) |
| 2459(43) | 58(3) | 0.24(5) | 0.16(2) | 2266(64) | 54(4) | 0.180(6) | 0.143(3) |
| 2552(44) | 59(3) | 0.11(1) | 0.101(4) | 2431(34) | 55(4) | 0.20(2) | 0.14(1) |
| 2574(55) | 59(3) | 0.092(8) | 0.091(3) | 2377(32) | 55(4) | 0.16(2) | 0.129(7) |
| 2655(80) | 59(3) | 0.11(1) | 0.094(4) | 2438(41) | 55(4) | 0.14(1) | 0.117(5) |
| 2695(54) | 59(3) | 0.082(7) | 0.083(3) | 2425(22) | 55(4) | 0.108(9) | 0.103(4) |
| 2640(93) | 59(3) | 0.079(7) | 0.083(3) | 2474(43) | 55(4) | 0.16(1) | 0.123(6) |
| 2642(89) | 59(3) | 0.14(1) | 0.108(6) | 2540(45) | 56(4) | 0.17(2) | 0.122(6) |
| 2813(53) | 60(3) | 0.0(0) | NA | 2635(48) | 56(4) | 0.12(1) | 0.102(4) |
| | | | | 2578(52) | 56(4) | 0.065(6) | 0.079(3) |
| | | | | 2586(33) | 56(4) | 0.13(1) | 0.105(4) |
| | | | | 2677(36) | 56(4) | 0.061(6) | 0.074(2) |
| | | | | 2717(20) | 57(4) | 0.068(6) | 0.076(3) |
| | | | | 2764(31) | 57(4) | 0.019(4) | 0.051(2) |
| | | | | 2842(19) | 57(4) | 0.0(0) | NA |

890

## Figure captions

**Figure 1:** SMS spectra and fitted effective thickness distributions of iron at 300 K and 1650 K at elevated pressures. Top panels: Synchrotron Mössbauer delayed counts (S) as a function of time (Eq. 3), from which the effective thickness ($\eta$) is fitted. Bottom panels: Best-fit probability density of effective thicknesses $\eta$ at different temperatures. The area integration under each curve is 1. The $\eta$ at higher temperature is expected to be smaller than $\eta$ at lower temperatures, because $f_{LM}$ decreases with temperature. The physical thickness of the sample changed less than 6% during the experiment, and the change in $\eta$ was dominated by the decrease of $f_{LM}$ with temperature.

**Figure 2:** Determination of the effective thicknesses at different temperatures using SMS delayed counts. The evolution of pressure with temperature is noted in Tab. 1. The pressures at 300 K are $47\pm3$ GPa for Run 1, and $44\pm4$ GPa for Run 2. The theoretical curves (right panels) are calculated using the effective thickness determined by the 1650 K SMS spectrum (Fig. 1) and Eq.4, and then scaled with the maximum value of the measured SMS delayed counts (left panels). The effective thickness for each temperature is determined by projecting the measured SMS delayed counts to the corresponding theoretical curves. The maximum value of the measured normalized delayed counts are different between runs, because of the temporal drift in incident resonant X-ray flux and the variations in sample thickness. Dashed curves in b) and d): error range of the theoretical curve calculated from Eq.4.

**Figure 3:** $f_{LM}$ of iron at different pressures and temperatures. Magenta diamonds, crosses and stars: $f_{LM}$ of $\alpha$-Fe measured at room pressure by Mauger et al. (2014), Bergmann et al. (1994) and

914 Chumakov et al. (1996), respectively. Magenta solid curve: $f_{LM}$ calculated from harmonic model
915 at 0 GPa. Red up triangles and green down triangles: $f_{LM}$ of $\gamma$- and $\epsilon$-Fe measured at high pressures
916 by Shen et al. (2004) and Lin et al. (2005), respectively. Number next to each triangle indicates its
917 pressure at 300 K. Blue circles and cyan squares: $f_{LM}$ determined by this study. Blue solid curve:
918 $f_{LM}$ calculated from the harmonic model at 50 GPa. Blue dotted line: $f_{LM}$ calculated from the
919 FLMT model. Black dashed line shows the $\gamma$-$\epsilon$ phase boundary of Fe at 50 GPa (Komabayashi et
920 al. 2009).

921

922 **Figure 4:** Equilibrium fractionation factor between $^{57}$Fe and $^{54}$Fe at different pressures and
923 temperatures. A) 1 bar data. Cyan squares: Mauger et al. (2014), calculated from the $f_{LM}$ data using
924 Eqs. 1 and 2. The $f_{LM}$ in Mauger et al. (2014) is calculated using the PHOENIX software package.
925 Magenta crosses: Mauger et al. (2014), calculated from the phonon DOS and the GM approach
926 (Polyakov, 2009; Dauphas et al. 2018). Black solid line: Polyakov (2009). Black dashed line: Liu
927 et al. (2017), recalculated using equation $10^3\ln\beta_{57/54} = 1.47 \times 10^3\ln\beta_{56/54}$ (Young et al. 2002). Red
928 solid line: β-factor calculated from harmonic approximation using Eqs. 1 and 2. Red dotted line:
929 β-factor calculated from harmonic approximation shifted down by 0.1‰ as a visual reference. B)
930 51-60 GPa data. Blue circles and cyan squares: iron β-factors determined by this study (Tab. 1).
931 Magenta square: Lin et al. (2005), calculated from the phonon DOS and the general moments
932 approach. Black solid line: 50 GPa data from Polyakov (2009). Black dashed line: 50 GPa data,
933 recalculated from Liu et al. (2017). Red solid line: β-factor calculated from the harmonic
934 approximation at 50 GPa. Red dotted line: β-factor calculated from harmonic approximation
935 shifted down by 0.1‰ as a visual reference. Cyan line: β-factor calculated from the 50 GPa FLMT
936 model. Shaded region: possible range for lnβ of Fe at temperatures above the melting point.

**Figure 5:** Equilibrium isotope fractionation β-factor between $^{57}$Fe and $^{54}$Fe at ambient pressure, determined from $f_{LM}$ (horizontal axis, this study) and the phonon DOS (vertical axis). Both the $f_{LM}$ and the phonon DOS are from Mauger et al. (2014). Black dashed line: Y = X identity line.

**Figure 6:** Equilibrium isotope fractionation β-factor between $^{57}$Fe and $^{54}$Fe in ε-Fe at simultaneous high P-T conditions calculated using GM method (Dauphas et al. 2012). Red solid line: $\ln\beta_{\mathrm{Fe}}^{57/54}$ calculated from GM model using force constant determined at 54.6 GPa and 300 K (325.6 N/m) (Dauphas et al. 2012). Red dotted line: $\ln\beta_{\mathrm{Fe}}^{57/54}$ calculated from GM model shifted down by 0.1‰ for the purpose of demonstration, truncated at 1700 K since experimental data above 1700 K is unavailable. Blue squares: $\ln\beta_{\mathrm{Fe}}^{57/54}$ calculated from GM model using force constants measured at simultaneous high P-T conditions from Lin et al. (2005). Coefficient $B_2$ from the Tab. 1 in Dauphas et al. (2012) is used in the calculation, and the blue number next to each data point indicates the pressure of each measurement. The lnβ calculated from the GM model using simultaneous high P-T force constant is systematically lower than the lnβ extrapolated from the GM model using room temperature force constant by at least 0.1‰.

Fig. 1

This is the peer-reviewed, final accepted version for American Mineralogist, published by the Mineralogical Society of America.
The published version is subject to change. Cite as Authors (Year) Title. American Mineralogist, in press.
DOI: https://doi.org/10.2138/am-2021-7884. http://www.minsocam.org/

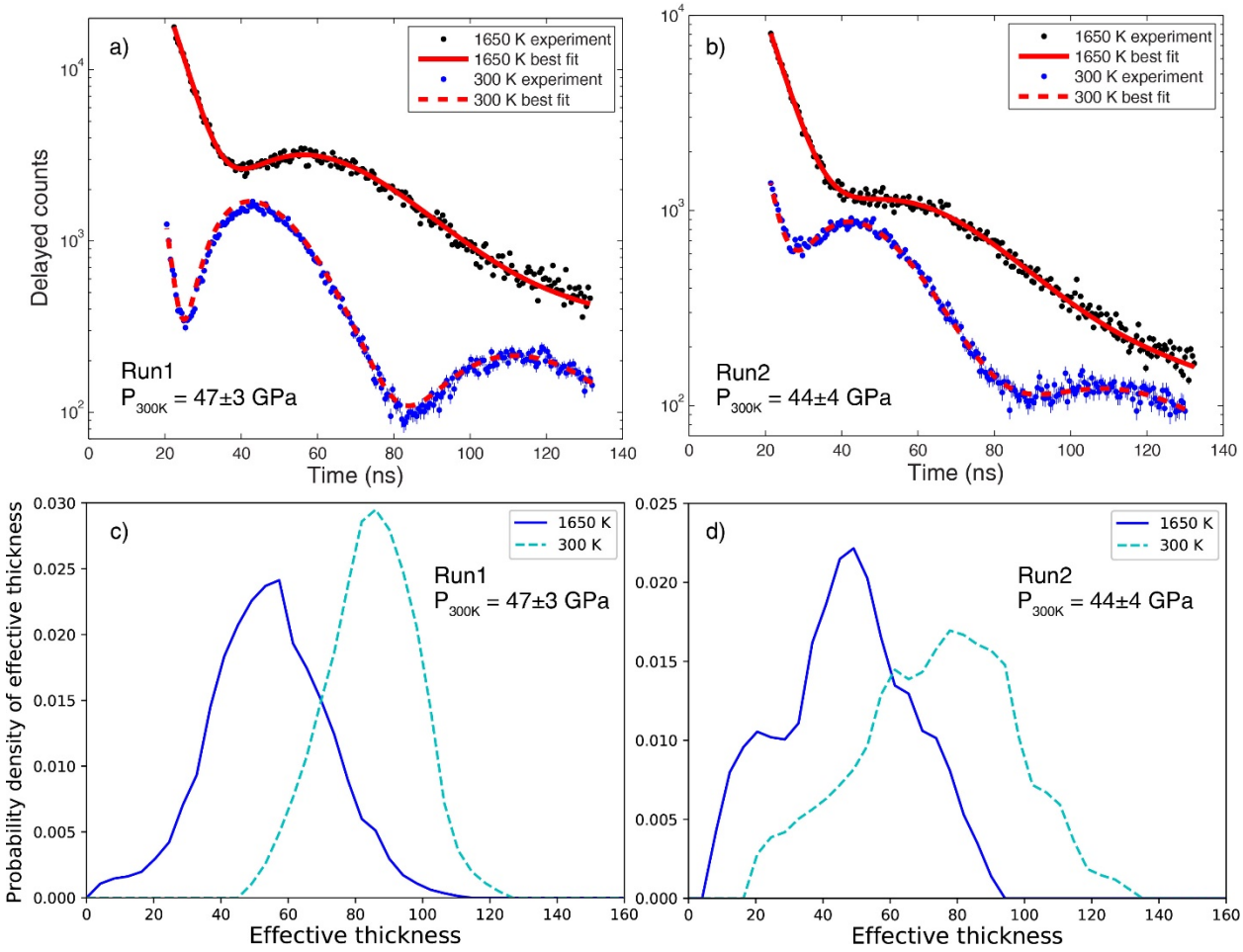


955

956

This is the peer-reviewed, final accepted version for American Mineralogist, published by the Mineralogical Society of America.
The published version is subject to change. Cite as Authors (Year) Title. American Mineralogist, in press.
DOI: https://doi.org/10.2138/am-2021-7884. http://www.minsocam.org/

957 Fig. 2

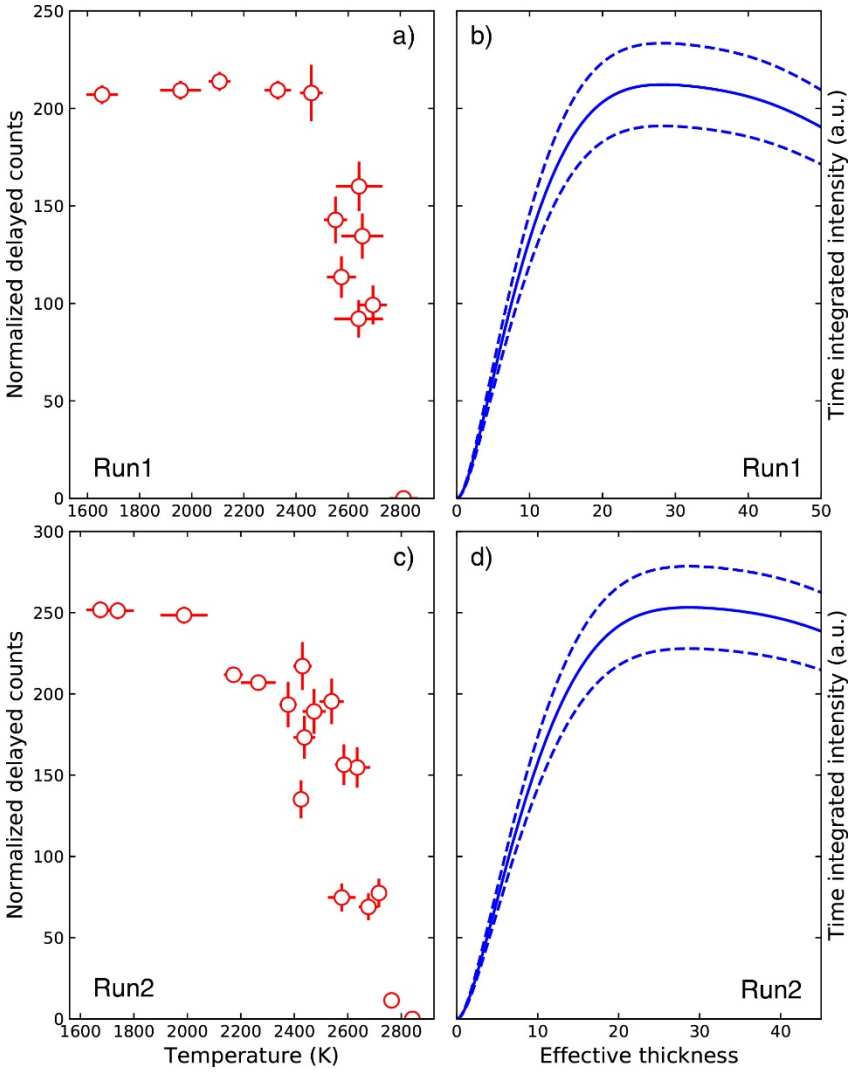


958

959

This is the peer-reviewed, final accepted version for American Mineralogist, published by the Mineralogical Society of America.
The published version is subject to change. Cite as Authors (Year) Title. American Mineralogist, in press.
DOI: https://doi.org/10.2138/am-2021-7884. http://www.minsocam.org/

960 Fig. 3

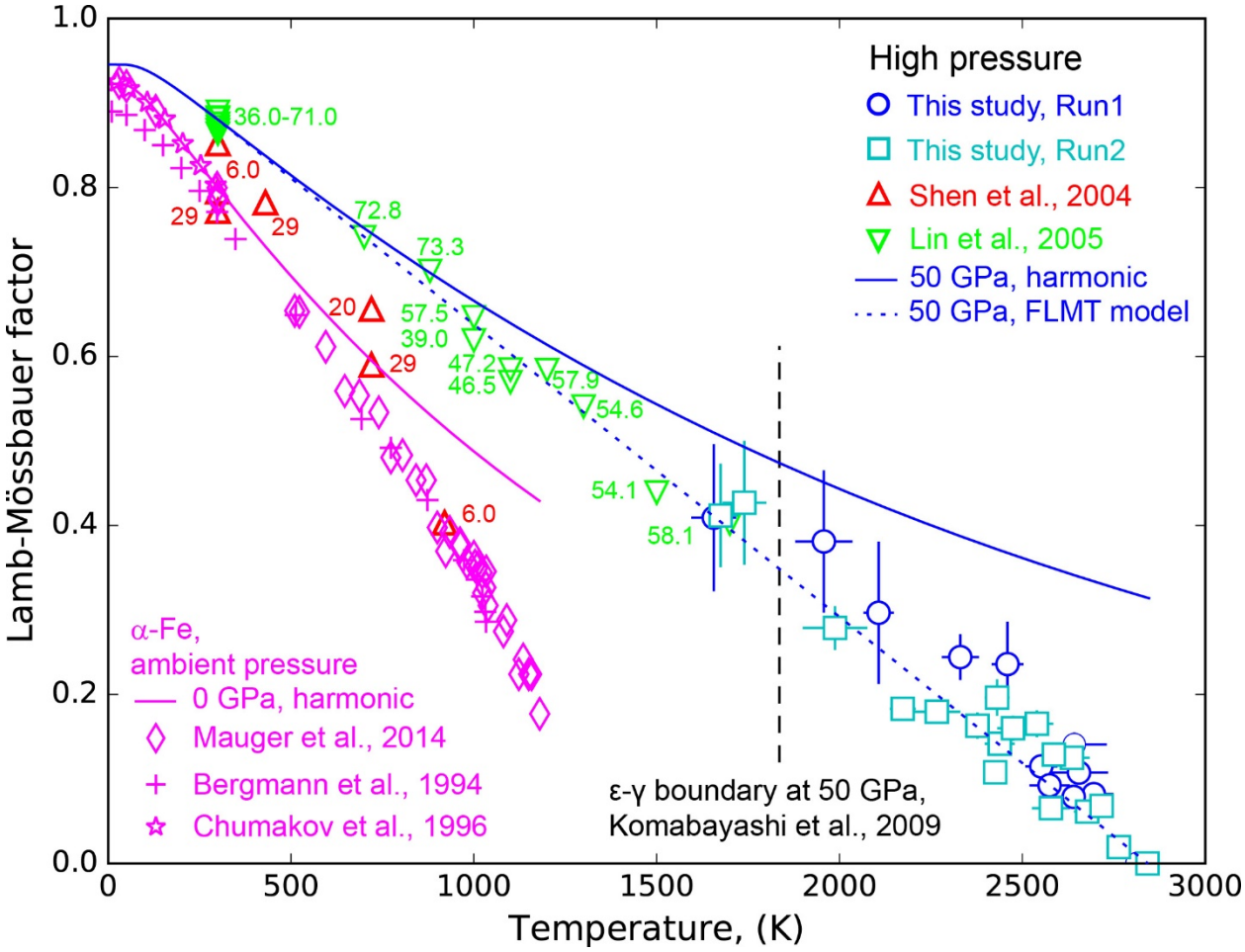


961

962

This is the peer-reviewed, final accepted version for American Mineralogist, published by the Mineralogical Society of America.
The published version is subject to change. Cite as Authors (Year) Title. American Mineralogist, in press.
DOI: https://doi.org/10.2138/am-2021-7884. http://www.minsocam.org/

963 Fig. 4

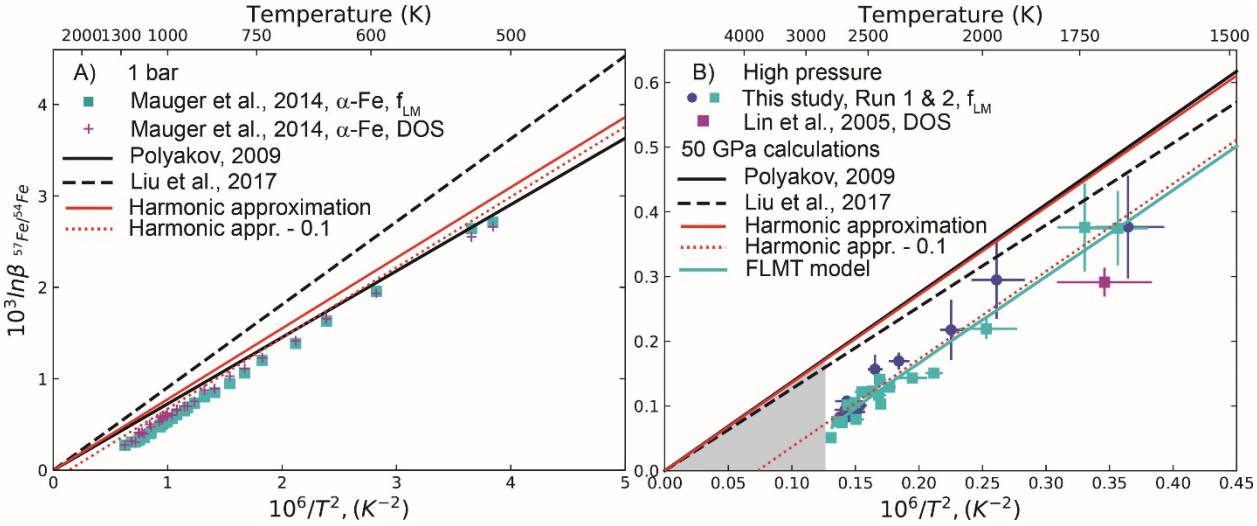


964

965

966 Fig. 5

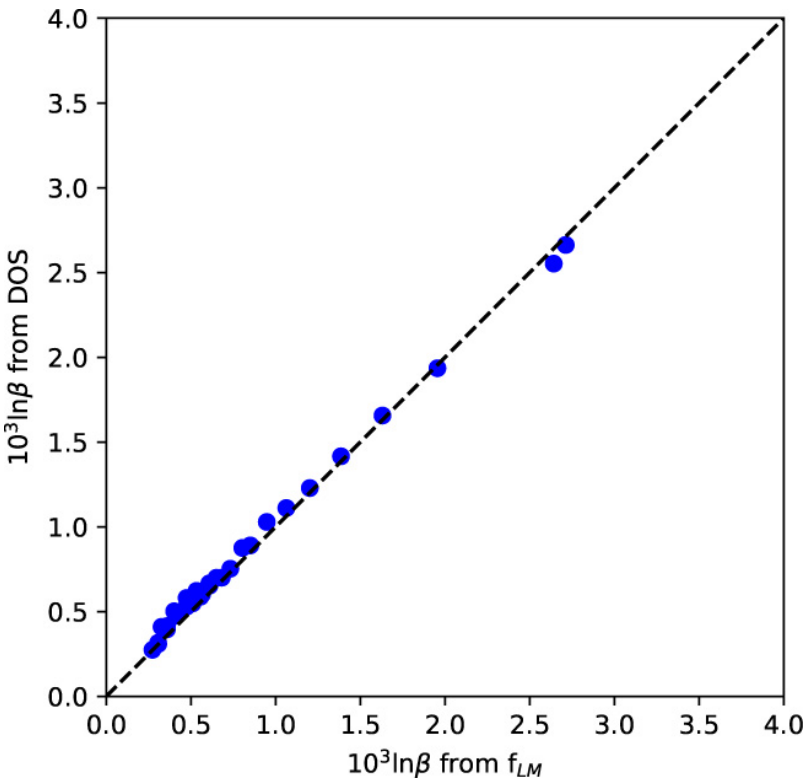


967

968

This is the peer-reviewed, final accepted version for American Mineralogist, published by the Mineralogical Society of America.
The published version is subject to change. Cite as Authors (Year) Title. American Mineralogist, in press.
DOI: https://doi.org/10.2138/am-2021-7884. http://www.minsocam.org/

969 Fig. 6

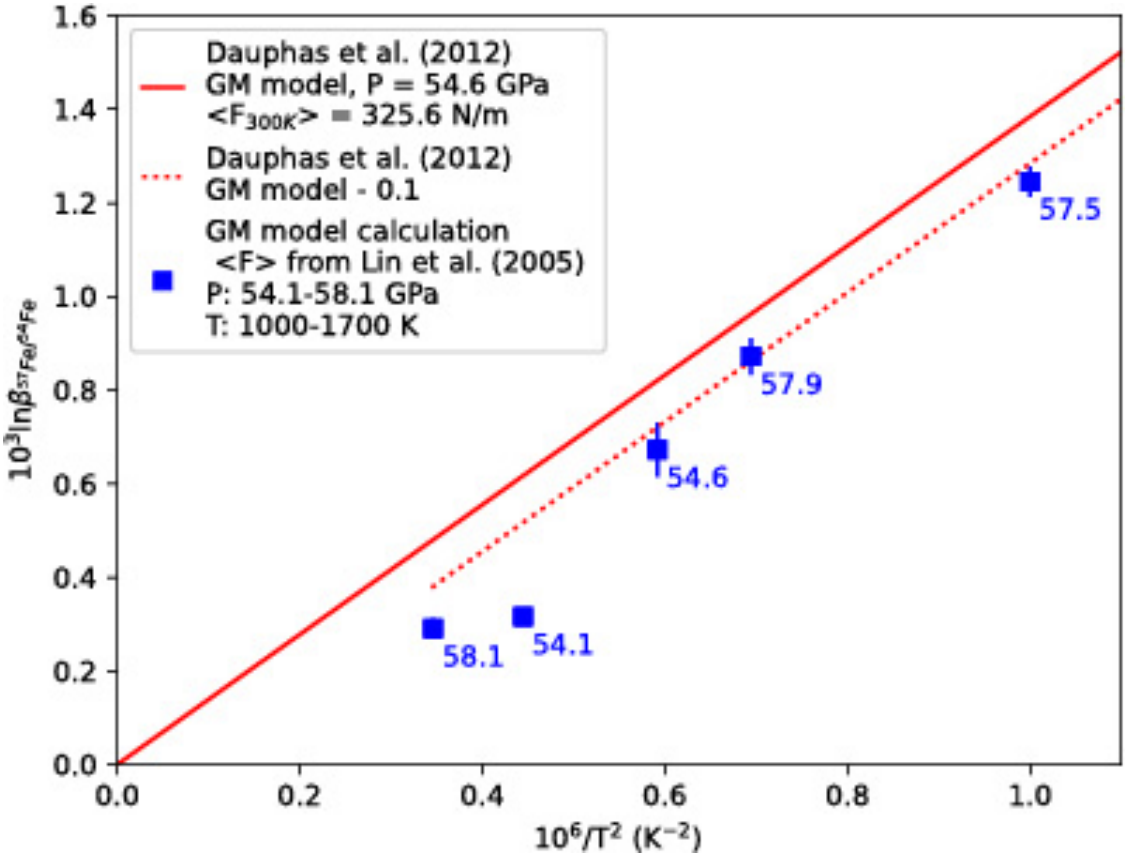


970